Comprehensive shear stress analysis of turbulent boundary layer profiles

Kristofer M. Womack[1]**, Charles Meneveau**[1]** and Michael P. Schultz**[2],†

[1]Department of Mechanical Engineering, Johns Hopkins University, Baltimore, MD 21218, USA

[2]Department of Naval Architecture and Ocean Engineering, United States Naval Academy, Annapolis, MD 21402, USA

Motivated by the need for accurate determination of wall shear stress from profile measurements in turbulent boundary layer flows, the total shear stress balance is analysed and reformulated using several well-established semi-empirical relations. The analysis highlights the significant effect that small pressure gradients can have on parameters deduced from data even in nominally zero pressure gradient boundary layers. Using the comprehensive shear stress balance together with the log-law equation, it is shown that friction velocity, roughness length and zero-plane displacement can be determined with only velocity and turbulent shear stress profile measurements at a single streamwise location for nominally zero pressure gradient turbulent boundary layers. Application of the proposed analysis to turbulent smooth- and rough-wall experimental data shows that the friction velocity is determined with accuracy comparable to force balances (approximately 1 %–4 %). Additionally, application to boundary layer data from previous studies provides clear evidence that the often cited discrepancy between directly measured friction velocities (e.g. using force balances) and those derived from traditional total shear stress methods is likely due to the small favourable pressure gradient imposed by a fixed cross-section facility. The proposed comprehensive shear stress analysis can account for these small pressure gradients and allows more accurate boundary layer wall shear stress or friction velocity determination using commonly available mean velocity and shear stress profile data from a single streamwise location.

Key words: turbulent boundary layers, boundary layer structure

1. Introduction

The turbulent boundary layer is ubiquitous, occurring commonly in both nature and engineering applications. It is important in geophysical flows where better weather prediction models require more accurate representations of surface layer physics and in transportation where drag reduction could lower fuel costs and greenhouse gas emissions. The most important physical quantity characterizing wall-bounded turbulent boundary layers is the skin friction drag. The topic of experimental determination of skin friction drag is closely linked to a fundamental understanding of the total

† Email address for correspondence: mschultz@usna.edu

momentum balance in turbulent boundary layers. Much has been learned over a long history of research on these related topics and reviews of various skin friction determination techniques can be found in Winter (1979), Haritonidis (1989), Klewicki *et al.* (2007) and Walker (2014).

The most widely used analysis techniques to determine skin friction are based on measurements of the streamwise mean velocity profile at various heights above the surface. The data are then compared to the assumed log-law equation (Clauser 1954) in order to estimate the friction velocity, roughness function and zero-plane displacement. The log-law equation reads

$$U^+ \equiv \frac{U}{u_\tau} = \frac{1}{\kappa} \ln \left[\frac{(y-d)u_\tau}{\nu} \right] + A - \Delta U^+. \tag{1.1}$$

In this equation U is the mean streamwise velocity, κ is the Kármán constant and A is the log-law intercept for smooth walls. The unknown scaling parameter is the friction velocity, u_τ, and the $+$ superscript indicates normalization by u_τ. When roughness is present, both d and ΔU^+ are non-zero and unknown as well. Here, d is a shift in the effective origin of the log law due to the roughness, and the roughness function, ΔU^+, models a change in the mean flow velocity due to the roughness. Case-by-case comparisons of these parameters remain an important way to describe differences among turbulent boundary layers. However, these parameters are difficult to determine accurately based on a single mean velocity profile due to the number of unknowns and possible dependencies between them.

Clauser was the first to use (1.1) to determine these parameters by fitting mean velocity profiles to the equation. He developed a graphical log-law fitting method for determining friction velocity and roughness function known as the Clauser chart method (Clauser 1954). Perry & Joubert (1963) extended this method for rough walls to include the shift in effective origin in what Perry & Li (1990) later termed the modified Clauser chart method.

There are clear shortcomings to these log-law fitting approaches. Perry & Joubert (1963) and Castro (2007) note that many different combinations of friction velocity, roughness function and effective origin can give equally good fits to experimental data. Also, Wei, Schmidt & McMurtry (2005) have shown that specific assumptions about the value of the Kármán constant and the fitting procedure used can often mask subtle dependencies on other variables such as the Reynolds number, *Re*. Nonetheless, many researchers still use fitting procedures due to the lack of a better alternative. To address the shortcomings of the fitting procedures, many researchers measure additional quantities in an attempt to reduce the number of unknowns for fitting.

The most important unknown is the friction velocity, u_τ, because it relates directly to the surface drag. Direct measurement of wall shear stress, which is related to friction velocity by $u_\tau \equiv \sqrt{\tau_w/\rho}$, is possible using a force balance among other methods. Sensitive floating element force balances have been successfully employed in many experiments such as Krogstad & Efros (2010), Baars *et al.* (2016) and Ferreira, Rodriguez-Lopez & Ganapathisubramani (2018). However, these balances are usually expensive, normally require careful surface preparation and alignment and typically only measure wall shear stress at a single downstream location in the experimental facility. These are significant challenges which limit the widespread experimental application of force balances, even at laboratories where they are available.

Friction velocity determination methods that require only fluid velocity measurements are necessary since direct, force balance measurement is not always feasible. Additionally, fluid velocity measurement methods can serve as cross-verification of direct measurement results. The traditional total shear stress method assumes that the

total shear stress near the wall is composed of only two significant components: the viscous shear stress and the Reynolds shear stress. This method was in common use by the mid-1980s and is still used presently (Li, Henbest & Perry 1986; Schultz & Flack 2007; Walker 2014). However, discrepancies between expected and measured results were noted early on. Initial investigations by Li *et al.* (1986) and Raupach, Antonia & Rajagopalan (1991) concluded that discrepancies were due to measurement limitations inherent in the hot-wire equipment utilized. Later studies by Cheng & Castro (2002) and Cheng *et al.* (2007), which compared direct measurement methods and laser Doppler velocimetry flow measurements, reasonably attributed the discrepancy to unmeasured fluid dynamic effects.

Several recent studies have attempted to quantify these previously unaccounted fluid dynamic effects including Fukagata, Iwamoto & Kasagi (2002), Mehdi & White (2011), Mehdi *et al.* (2014) and Volino & Schultz (2018). These shear stress methods attempt to quantify additional measurable shear stress terms by using the Reynolds-averaged, streamwise momentum equation for two-dimensional flows. These methods require additional fluid velocity measurements or assumptions for unknown or uncertain information. For example, Mehdi & White (2011) and Mehdi *et al.* (2014) are able to calculate friction velocity based on the measured streamwise mean velocity and Reynolds shear stress profiles. However, they find that the method is sensitive to unknown and noisy data near the wall. They overcome this limitation by assuming a shape for the total shear stress profile and by smoothing the measured data. Volino & Schultz (2018) derive a transformed version of the Reynolds-averaged, streamwise momentum equation for two-dimensional flows. They are then able to calculate friction velocity based on the measured streamwise velocity and Reynolds shear stress profiles. However, multiple streamwise profile locations are required because some significant terms are affected by streamwise gradients.

The complexity of these methods, the required high and often impractical experimental accuracy and the lack of required data pose a barrier for common adoption. Left with a difficult problem, recent studies by Reynolds & Castro (2008) and Placidi & Ganapathisubramani (2015) have concluded that traditional total shear stress methods require an evidence-based adjustment of approximately 12 % in order to match direct (force balance) wall stress measurements.

The present paper aims to develop a more complete understanding of each of the terms in the momentum equation and to approximate missing terms using well-established semi-empirical relations and non-dimensionalizations. These insights enable the development of a more comprehensive shear stress method that improves the agreement with direct wall stress measurements and circumvents the need for empirical *a posteriori* adjustments to the wall stress calculated with fluid velocity and shear stress profile measurements. The proposed comprehensive shear stress method requires no more data than traditional total shear stress methods and aims to describe the turbulent shear stress throughout much of the boundary layer. Increased utility with less data is accomplished by extending the Volino & Schultz (2018) equation and supplementing it with semi-empirically justified assumptions about the streamwise development of a boundary layer.

It is shown that coupling this new friction velocity equation with log-law fitting provides an accurate method for determining friction velocity in nominally zero pressure gradient boundary layers. The accuracy of the method is demonstrated on several recent data sets including Cheng & Castro (2002) which is often cited for demonstrating this discrepancy between traditional total shear stress methods and direct measurements. The proposed new method reasonably accounts for the

discrepancy by demonstrating the effect of a small favourable pressure gradient caused by a fixed tunnel cross-section on turbulent shear stress and avoids the need for empirical adjustment of experimental data. The improved accuracy in friction velocity determination demonstrates the importance of including as many of the terms affecting the mean momentum balance as possible.

Section 2 describes the reformulated momentum balance in developing boundary layers and tests the accuracy of the proposed form using various shear stress data sets. Also, an iterative method to combine this analysis with the log-law equation for the mean velocity is described. The comprehensive shear stress method is then applied to several recent experimental data sets in §3 to demonstrate the performance of the proposed method of analysis, leading to more accurate friction velocity determination. Results are summarized in §4, and conclusions are presented in §5.

2. Method

The present approach is based on two equations which can be fit to the mean streamwise velocity profile and the Reynolds shear stress profile in zero or nominally zero pressure gradients. The two equations each have dependencies on friction velocity and roughness function which allow iterative convergence to a unique result for friction velocity, roughness function and zero-plane displacement.

The first equation is an extension to the Volino & Schultz (2018) equation which allows calculation of friction velocity. Section 2.1 presents the derivation of this extended Volino & Schultz equation which calculates friction velocity, u_τ, maintains the advantages of the original method and expands its applicability by adding dispersive shear stress and allowing calculation of streamwise gradients from a single two-component profile. The second equation is the log-law equation for the mean velocity. Section 2.2 describes the fitting of the log-law equation. Roughness function and zero-plane displacement are calculated by a two-parameter fit of the overlap region of the boundary layer mean velocity profile. Section 2.3 summarizes the comprehensive shear stress method and the iterative approach combining both equations.

2.1. *Rescaled mean momentum balance equation*

For steady, two-dimensional flow with constant properties, the integral form of the Reynolds-averaged and spatially averaged streamwise momentum equation is

$$\frac{\tau_w}{\rho} - \left(\nu \frac{\partial \langle U \rangle}{\partial y} - \langle \overline{u'v'} \rangle - \langle \tilde{u}\tilde{v} \rangle \right) + \frac{1}{\rho} \frac{\mathrm{d} \langle P \rangle}{\mathrm{d} x} y$$
$$-\langle U \rangle \int_0^y \frac{\partial \langle U \rangle}{\partial x} \,\mathrm{d}y + 2 \int_0^y \langle U \rangle \frac{\partial \langle U \rangle}{\partial x} \,\mathrm{d}y + \int_0^y \frac{\partial \langle \overline{u'^2} \rangle}{\partial x} \,\mathrm{d}y = 0, \qquad (2.1)$$

when integrated from the wall to any arbitrary height, y. Here, x and y are the streamwise and wall-normal directions, and U and V are the time-averaged streamwise and wall-normal velocities, respectively. Here, τ_w is the wall shear stress, ρ is the density, ν is the kinematic viscosity, P is the pressure, $-\overline{u'v'}$ is the Reynolds shear stress and $\overline{u'^2}$ is the streamwise Reynolds normal stress. The overbars denote time averaging, and the angle brackets denote spatial averaging. The primes denote time fluctuating components from the Reynolds decomposition, $u = U + u'$, and tildes denote spatially fluctuating components from a further spatial average decomposition, $U = \langle U \rangle + \tilde{u}$.

For boundary layer profiles, spatial averaging of multiple data points at the same wall-normal distance, y, can be advantageous. The most common context for such averaging is particle image velocimetry where time-averaged statistics from a two-dimensional vector field may be further spatially averaged into a single better converged one-dimensional profile. Examples of this approach can be found in Nakagawa & Hanratty (2001), Wu & Christensen (2007) and Placidi & Ganapathisubramani (2015). Additionally, spatial averaging may be important for hot-wire or laser Doppler velocimetry measurements as well. Cheng & Castro (2002) and Cheng *et al.* (2007) studied several urban-like roughnesses. They measured several cross-wire anemometry profiles over a single repeating unit for each surface. The spatially averaged profile was then a more representative profile which could be considered homogeneous on scales larger than the repeating unit itself for each surface.

Equation (2.1) can be used to calculate τ_w directly as was done successfully by Brzek *et al.* (2007) in a zero pressure gradient (ZPG) boundary layer. However, Volino & Schultz (2018) noted that its accuracy depends largely on the ability to accurately measure the streamwise gradient terms. This is difficult given experimental constraints and uncertainties in most circumstances. To mitigate this challenge, Volino & Schultz (2018) transformed the equation to wall coordinates in the wall-normal, y-direction, only and separate the streamwise gradient terms into various groups. They use the standard definitions for non-dimensional terms

$$y^+ = \frac{yu_\tau}{\nu}, \quad U^+ = \frac{U}{u_\tau}, \quad \overline{u'v'}^+ = \frac{\overline{u'v'}}{u_\tau^2}, \quad \overline{u'^2}^+ = \frac{\overline{u'^2}}{u_\tau^2}, \quad \frac{1}{\rho}\frac{dP}{dx} = -\frac{KU_e^3}{\nu},$$
$$K = \frac{\nu}{U_e^2}\frac{dU_e}{dx} \quad \text{and} \quad \frac{c_f}{2} = \left(\frac{u_\tau}{U_e}\right)^2, \tag{2.2}$$

where U_e is the free-stream velocity, K is the acceleration parameter and c_f is the skin friction. Equation (2.1) can be rewritten in the transformed variables as follows:

$$-\langle\overline{u'v'}\rangle^+ - \langle\tilde{u}\tilde{v}\rangle^+ = 1 - \underbrace{\frac{\partial\langle U\rangle^+}{\partial y^+}}_{\text{I}} - \underbrace{\frac{K}{(c_f/2)^{3/2}}y^+}_{\text{II}}$$

$$+ \underbrace{\left[\frac{K}{\sqrt{c_f/2}} + \frac{\nu}{U_e(c_f/2)}\frac{d\sqrt{c_f/2}}{dx}\right]\int_0^{y^+}\langle U\rangle^{+2}\,dy^+}_{\text{III}}$$

$$+ \underbrace{\frac{\nu}{U_e\sqrt{c_f/2}}\left(2\int_0^{y^+}\langle U\rangle^+\frac{\partial\langle U\rangle^+}{\partial x}\,dy^+ - \langle U\rangle^+\int_0^{y^+}\frac{\partial\langle U\rangle^+}{\partial x}\,dy^+\right)}_{\text{IV}}$$

$$+ \underbrace{\left[\frac{K}{\sqrt{c_f/2}} + \frac{\nu}{U_e(c_f/2)}\frac{d\sqrt{c_f/2}}{dx}\right]\left(y^+\langle\overline{u'^2}\rangle^+ + \int_0^{y^+}\langle\overline{u'^2}\rangle^+\,dy^+\right)}_{\text{V}}$$

$$+ \underbrace{\frac{\nu}{U_e\sqrt{c_f/2}}\int_0^{y^+}\frac{\partial\langle\overline{u'^2}\rangle^+}{\partial x}\,dy^+}_{\text{VI}}. \tag{2.3}$$

Equation (2.3) is the extended Volino & Schultz equation and differs from that of Volino & Schultz (2018) in that the spatial averaging operators, $\langle \cdots \rangle$, and the dispersive stress term, $-\langle \tilde{u}\tilde{v} \rangle^+$, are included here. The dispersive stress term arises because of the spatial averaging and becomes significant when time-averaged velocities vary significantly over the area being spatially averaged.

Terms in (2.3) are ordered according to their relative significance in the near-wall region as in Volino & Schultz (2018). For turbulent smooth-wall data from Morrill-Winter *et al.* (2015), Volino & Schultz (2018) found that term I was the only significant term from the wall to $y/\delta = 0.04$, term II is zero for ZPG flow, terms I and III are the only significant terms up to $y/\delta = 0.2$ and terms I, III and IV provided a good fit to data up to $y/\delta = 0.4$. In the above ranges, wall-normal distance was normalized by boundary layer thickness, δ. Terms V and VI are derived from the Reynolds normal stress term and have been found to be insignificant (Volino & Schultz 2018).

The goal of the derivation presented next is to extend the usefulness of (2.3) to experiments where data from only a single streamwise location are available. This requires that terms with streamwise gradients are reformulated so that they may be calculated indirectly using only the velocity profile data from a single streamwise location, rather than directly by using multiple profiles as in Volino & Schultz (2018). The derivation that follows will consider only nominally ZPG boundary layers. Additionally, terms V and VI have been found to be insignificant and will subsequently be neglected (Volino & Schultz 2018).

2.1.1. *Determining the friction velocity gradient*

Term III contains the streamwise friction velocity gradient, $(d/dx)\sqrt{c_f/2}$, or equivalently, $(d/dx)(u_\tau/U_e)$. This term is of primary concern because Volino & Schultz (2018) have shown that it is significant for determining u_τ from data between approximately $0.04 \leqslant y/\delta \leqslant 0.2$. This is also the region where there is the best chance of accurately determining u_τ from (2.3) because experimental Reynolds shear stress measurements are more accurate outside of the immediate vicinity of the wall and because experimental errors which may build up in the integrals of terms III and IV are minimized. A convenient reformulation of this term is possible through the skin friction law and the momentum integral equation (MIE) by extending work of Clauser (1954), Rotta (1962) and Castro (2007). The derivation is more easily completed using an alternate form of (1.1) (expressed with the roughness length) and the wake function

$$U^+ \equiv \frac{U}{u_\tau} = \frac{1}{\kappa} \ln \left(\frac{y}{y_0} \right) + \frac{\Pi}{\kappa} W \left(\frac{y}{\delta} \right). \tag{2.4}$$

Roughness length, y_0, is related to ΔU^+ by

$$\Delta U^+ = A + \frac{1}{\kappa} \ln \left(\frac{y_0 u_\tau}{\nu} \right). \tag{2.5}$$

In velocity-defect form, equation (2.4) is

$$\frac{U_e - U}{u_\tau} = -\frac{1}{\kappa} \ln \left(\frac{y}{\delta} \right) + \frac{\Pi}{\kappa} \left(2 - W \left(\frac{y}{\delta} \right) \right). \tag{2.6}$$

The addition of the wake function, $W(y/\delta)$, to model the outer flow was first proposed by Coles (1956). The wake function is normalized so that the wake

strength parameter, Π, accurately characterizes the strength of the wake relative to other turbulent boundary layers. This paper will use the most common definition of the boundary layer thickness, δ, namely the wall-normal distance where velocity reaches 99 % of the free-stream velocity (so that $U(\delta) = 0.99U_e$). Coles (1956) does not utilize this definition of δ but rather defines it based on normalizing conditions for the wake function. Therefore, Coles' δ is approximately 10 % to 30 % larger than the 99 % δ depending upon the specific wake function. Additionally, Coles (1956) hypothesized that $W(y/\delta)$ is a universal function. This allowed him to define Π by the normalizing conditions as well. In an effort to avoid the assumption of a universal wake function in this work, Π will be defined by the wake function's maximum departure from the extrapolated log law so that

$$\Pi = \frac{\kappa}{2} \max \left[U^+(y) - \frac{1}{\kappa} \ln \left(\frac{y}{y_0} \right) \right]. \tag{2.7}$$

This approach also avoids the wake strength's definition being tied to any single definition of boundary layer thickness while the maximum deviation typically still occurs very near the 99 % δ (so that $W_{\max}(y/\delta \approx 1) = 2$).

Assuming that (2.4) and (2.6) accurately model a turbulent boundary layer velocity profile in an overlap region, Clauser (1954) and Rotta (1962) both show that a skin friction law is derived from substituting (2.4) into (2.6). The result is

$$\frac{U_e}{u_\tau} = \frac{1}{\kappa} \ln \left(\frac{\delta}{y_0} \right) + \frac{2\Pi}{\kappa}. \tag{2.8}$$

Equation (2.8) is the skin friction law but is not yet expressed in more customary terms with the local skin friction and momentum thickness. In order to do that, recall that $c_f/2 \equiv (u_\tau/U_e)^2$ and shape factor, $H \equiv \delta^*/\theta$, where δ^* is the displacement thickness and θ is the momentum thickness.

If the definition of displacement thickness is applied to (2.6), δ^* is related to δ by

$$\frac{\delta^*}{\delta} \frac{U_e}{u_\tau} = \frac{\delta^*}{\delta} \sqrt{\frac{2}{c_f}} = \frac{1 + \Pi \left[2 - \int_0^\delta W d(y/\delta) \right]}{\kappa} \approx \frac{1 + \Pi}{\kappa}. \tag{2.9}$$

Coles (1956) imposed $\int_0^1 W \, d(y/\delta) = 1$ as one of the wake function normalization criteria and derived the final expression on the right with exact equivalence. Here, $\int_0^1 W \, d(y/\delta) = 1$ is assumed (rather than imposed) for the standard definition of δ, which for ZPG boundary layer flows is of sufficient accuracy for present purposes. With these relations, the skin friction law, equation (2.8), can be rewritten as in Castro (2007) according to

$$\sqrt{\frac{2}{c_f}} = -\frac{1}{\kappa} \ln \left(\frac{1}{H} \sqrt{\frac{c_f}{2}} \right) + \frac{1}{\kappa} \ln \left(\frac{\theta}{y_0} \right) + K_\Pi, \tag{2.10}$$

where $K_\Pi = 2\Pi/\kappa - (1/\kappa) \ln [(1 + \Pi)/\kappa]$. Castro further showed that this expression can be rearranged to

$$\frac{\theta}{y_0} = \frac{s - I}{s^2} e^{\kappa(s - K_\Pi)}, \tag{2.11}$$
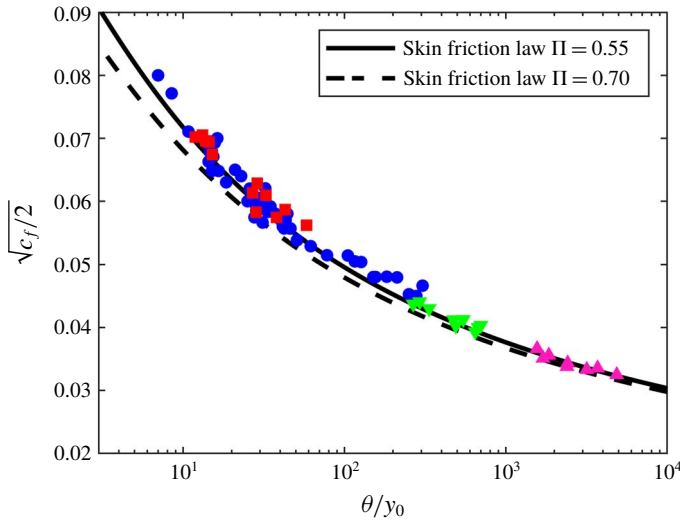
FIGURE 1. (Colour online) Skin friction law modelled by (2.11) with experimental data from multiple sources. Blue circles (●) indicate Castro (2007) mesh, cubes, rectangular blocks and sand-grain surfaces, magenta up triangles (▲) indicate Morrill-Winter *et al.* (2015) smooth-wall surfaces, green down triangles (▼) indicate Squire *et al.* (2016) P36 sandpaper surfaces and red squares (■) indicate Placidi & Ganapathisubramani (2015) LEGO® block surfaces.

where $s = \sqrt{2/c_f}$ and I is Clauser's integral parameter (defined as G in Clauser (1954)). It is defined as

$$I = \int_0^\infty \left(\frac{U_e - U}{u_\tau} \right)^2 dy \bigg/ \int_0^\infty \frac{U_e - U}{u_\tau} dy = \frac{H-1}{H} \sqrt{\frac{2}{c_f}}. \qquad (2.12)$$

Here, I can be calculated from the measured velocity profile using (2.12). However, to test the validity of (2.11), it is convenient to assume a particular functional shape for the wake function, $W(y/\delta)$, so that I can be expressed as a function of Π only. Castro (2007) showed that $I(\Pi) = (2 + 3.2\Pi + 1.522\Pi^2)/[\kappa(1 + \Pi)]$ for Coles' wake function. Using this expression for I, it is then possible to plot (2.11) together with experimental data to test its validity because $\sqrt{c_f/2}$ remains a function of only θ/y_0 and Π.

Figure 1 shows $\sqrt{c_f/2}$ versus θ/y_0, as determined implicitly via (2.11) with $\Pi = 0.55$ and $\Pi = 0.70$, plotted together with recent experimental data. For the plotted curves, $I(\Pi)$ is calculated using Castro's expression for Coles' wake function, but it can be shown that the particular choice of ZPG wake function has minimal effect on the plotted curve. The experimental data show that (2.11) models a wide variety of surfaces quite well, from smooth to various types of rough surfaces. For instance, data from Morrill-Winter *et al.* (2015) are from smooth surfaces, Squire *et al.* (2016) are from sand-grain surfaces, Placidi & Ganapathisubramani (2015) are from LEGO® block surfaces and Castro (2007) are from mesh, cubes, rectangular blocks and sand-grain surfaces.

Figure 1 also shows that $\Pi = 0.55$ appears to model the data more closely than $\Pi = 0.70$. This is expected at lower skin frictions but interesting at higher

skin frictions. Since higher skin frictions are generally those with more aggressive roughness which generally have larger wake strengths (Keirsbulck *et al.* 2002), one would expect the experimental data to match the $\Pi = 0.70$ curve more closely at higher skin frictions. This deviation from the expectation may be due to the assumption $\int_0^1 W \, d(y/\delta) = 1$ which led to the approximate expression of (2.9) being used in the subsequent derivation. The authors have tried various definitions of δ to evaluate the integral explicitly; however, none of these efforts yielded a better agreement with the experimental data in figure 1. If this is true, it may be best to assume a value of $\Pi = 0.55$ in (2.11) regardless of the actual measured value from (2.7). However, the deviation may also be due to the small favourable pressure gradient imposed by the fixed cross-section tunnels used in both Castro (2007) and Placidi & Ganapathisubramani (2015). This small favourable pressure gradient would tend to reduce the wake strength causing these data points to potentially follow a lower wake strength curve. Due to the ambiguity, the present work uses Π calculated by (2.7) rather than an assumption at each step in the solution process. There is one exception explicitly documented for comparison in figure 5.

The ultimate goal of this derivation is to calculate the friction velocity gradient, $(d/dx)\sqrt{c_f/2}$. Now that a clear relationship between $\sqrt{c_f/2}$ and θ/y_0 has been demonstrated (note that (2.11) defines an implicit equation for $s = \sqrt{2/c_f}$ as function of θ/y_0), it remains to link θ with x. For ZPG boundary layers, the classical momentum integral analysis yields such a link, namely $c_f/2 = d\theta/dx$ (see also Castro (2007)). It follows that

$$
\frac{d\sqrt{c_f/2}}{dx} = \frac{\frac{d}{ds}\sqrt{c_f/2}}{dx/ds} = -\frac{e^{-\kappa(s-K_\Pi)}}{y_0 s^2}\left[1 + (s-I)\left(\kappa - \frac{2}{s}\right)\right]^{-1}, \qquad (2.13)
$$

where $(d/ds)\sqrt{c_f/2} = -1/s^2$ and $dx/ds = s^2 \, d\theta/ds$ have been used.

Equation (2.13) shows that $(d/dx)\sqrt{c_f/2} = f(s, y_0, \Pi, I)$ and provides a condition relating these quantities that will be used as part of an iterative process. Initially, u_τ and y_0 (and therefore s from U_e/u_τ, Π from (2.7), and I from (2.12)) may be unknown, but an initial guess of approximate values for these quantities may be obtained from the measured velocity profile and then further refined iteratively as described in § 2.3.

2.1.2. *Determining the velocity gradient profile*

Term IV from (2.3) contains the streamwise velocity gradient profile, $\partial\langle U\rangle^+/\partial x|_{y^+}$. By making evidence-based assumptions about the streamwise development of the boundary layer, it is possible to evaluate this term from a single mean velocity profile. Empirical evidence supporting the steps to follow are provided from studies such as Castro (2007), Sillero, Jiménez & Moser (2013), Morrill-Winter *et al.* (2015) and Squire *et al.* (2016). Starting from (2.4) and taking a derivative with respect to x yields

$$
\frac{\partial\langle U\rangle^+}{\partial x}\bigg|_{y^+} = \frac{1}{\kappa}\frac{\partial}{\partial x}\left[\ln\left(\frac{y}{y_0}\right)\right]_{y^+} + \frac{W}{\kappa}\frac{\partial\Pi}{\partial x} + \frac{\Pi}{\kappa}\frac{\partial}{\partial x}\left[W\left(\frac{y}{\delta}\right)\right]_{y^+}. \qquad (2.14)
$$

The first term can be neglected by recognizing that $y/y_0 = y^+/y_0^+$ and hence that $(\partial/\partial x)[\ln(y/y_0)]_{y^+} = 0$ if $\partial y_0^+/\partial x = 0$. From (2.5), the latter condition is equivalent to

assuming that ΔU^+ and A are independent of x, which is consistent with the empirical evidence that a set of normalized profiles separated by a streamwise distance over a homogeneous surface collapses in the log-law region once the flow is fully developed. This can be seen also in figure 2(a) on both smooth- and rough-wall data sets. Thus the streamwise gradient of the logarithmic term, $(\partial/\partial x)[\ln(y/y_0)]_{y^+}$, can be neglected.

The second term in (2.14) is discussed next. Careful examination of currently available sources yielded no theory or experimental fit which allowed the magnitude of $\partial \Pi/\partial x$ to be calculated accurately for a generic boundary layer. It is clear from Sillero *et al.* (2013) that this term is positive at low Reynolds numbers and becomes negligible in fully developed smooth-wall turbulent boundary layers above about $Re_\theta \gtrsim 6000$. It should also be negligible for any fully rough turbulent boundary layer.

The remaining term contains $\partial W/\partial x$. The strategy for evaluating this term with a mean streamwise velocity profile from only one streamwise location is to link it with $d\theta/dx$ through the chain rule. Defining $\eta = y/\delta$, the derivative becomes

$$
\frac{\partial}{\partial x}\left[W\left(\frac{y}{\delta}\right)\right]_{y^+} = \frac{dW}{d\eta}\frac{\partial}{\partial x}\left[\frac{y^+}{\delta^+}\right]_{y^+} = \frac{dW}{d\eta}\left(\frac{-y^+}{\delta^{+2}}\right)\frac{\partial \delta^+}{\partial x}
$$
$$
= \left(-\frac{y^+}{\delta^{+2}}\right)\left(\frac{u_\tau}{\nu}\frac{d\delta}{d\theta}\frac{d\theta}{dx} + \frac{\delta}{\nu}\frac{du_\tau}{dx}\right)\frac{dW}{d\eta}. \quad (2.15)
$$

The relation, $c_f/2 \equiv (u_\tau/U_e)^2$, can be substituted to obtain a result consistent with the terms of (2.3). Also, an additional relation is required for $d\delta/d\theta$. An approximation of this term can be found by noting that the plots seen in figures 2(b) and 2(c) of streamwise velocity profiles in the form of U/U_e versus y/δ from Morrill-Winter *et al.* (2015) and Squire *et al.* (2016) nearly collapse under this scaling. These velocity profiles are separated by a streamwise distance of approximately 20δ. A δ-scale differential streamwise distance would be expected to show even better collapse. This gives evidence that the integral $\int_0^\infty U/U_e(1 - U/U_e)\,d\eta$ is approximately constant. Noting

$$
\int_0^\infty \frac{U}{U_e}\left(1 - \frac{U}{U_e}\right)d\left(\frac{y}{\delta}\right) = \frac{1}{\delta}\int_0^\infty \frac{U}{U_e}\left(1 - \frac{U}{U_e}\right)dy = \frac{\theta}{\delta} \approx C, \quad (2.16)
$$

it may be concluded that δ/θ is approximately constant and thus equal to $d\delta/d\theta$. The momentum thickness grows proportionally with the boundary layer thickness for a fully developed boundary layer. This is consistent with often cited derivations from Schlichting (1979) in which a $1/7$ power-law model was used to derive $\theta/\delta = 7/72$. The difference here is that, instead of assuming a velocity profile model, the data from the measured profile can be used to approximate the ratio. Momentum and boundary layer thickness are again assumed to grow proportionally over a differential streamwise distance, and the measured δ/θ is substituted for $d\delta/d\theta$.

The above substitutions result in the final expression

$$
\left.\frac{\partial \langle U\rangle^+}{\partial x}\right|_{y^+} = -\frac{\Pi y}{\kappa\delta}\left[\frac{1}{\theta}\frac{d\theta}{dx} + \sqrt{\frac{2}{c_f}}\frac{d\sqrt{c_f/2}}{dx}\right]\frac{dW}{d\eta}
$$
$$
= -\frac{\Pi y^+}{\kappa}\left[\frac{1}{\theta}\frac{d\theta}{dx} + \sqrt{\frac{2}{c_f}}\frac{d\sqrt{c_f/2}}{dx}\right]\frac{\partial W}{\partial y^+}. \quad (2.17)
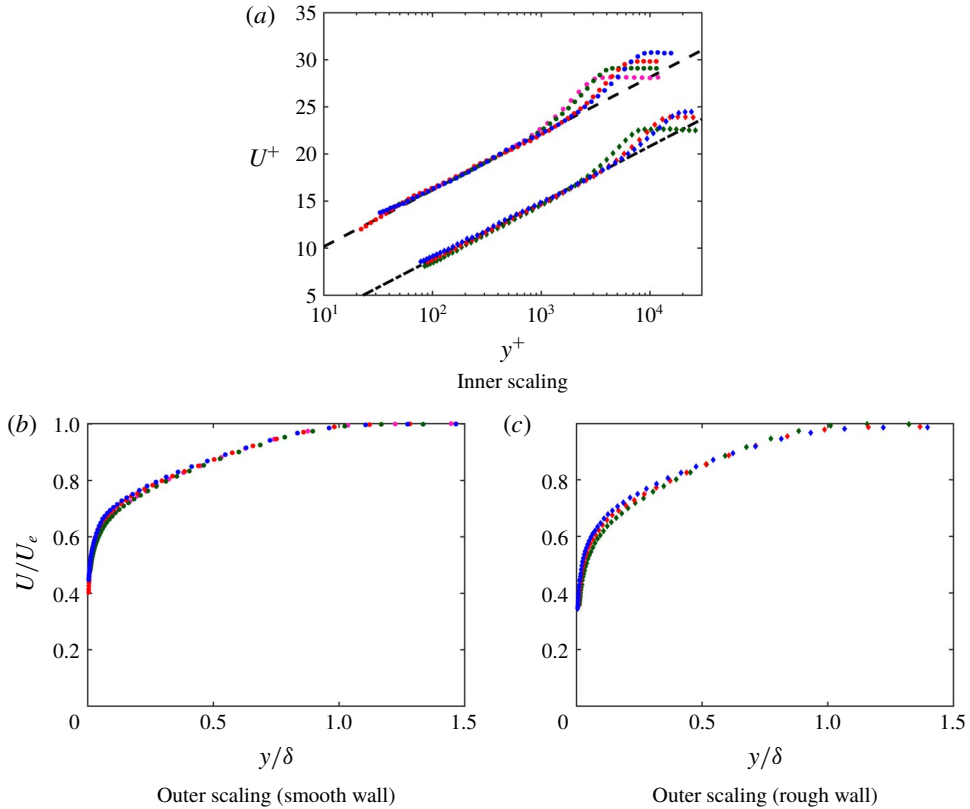$$

FIGURE 2. (Colour online) Scaled boundary layer profiles developing over increasing fetch. Circles (●) are from Morrill-Winter *et al.* (2015) smooth surface, and diamonds (◆) are from Squire *et al.* (2016) sandpaper surface. Profile locations are magenta at $x = 4.5$ m, green at $x = 7.0$ m, red at $x = 11.9$ m and blue at $x = 18.0$ m. Black dashed line is the smooth-wall log law, and black dash-dot line is the rough-wall log law.

The first term in brackets captures the effect of boundary layer growth (note that (2.15) requires that W scales with δ), and the second term arises because the vertical length scale changes as u_τ changes with fetch. The magnitude of these two terms can be easily compared for ZPG flows adding some insight. The bracketed part of the equation is equivalently $\theta^{-1}d\theta/dx + (1/2)(d\theta/dx)^{-1}d^2\theta/dx^2$. Using the well-known scaling $\theta \sim x^{4/5}$ for turbulent boundary layers, the first term in the brackets is about eight times larger than the second and has an opposite sign. The changing length scale has an order of magnitude smaller effect on the derivative when compared to the boundary layer's growth.

The ZPG MIE is $d\theta/dx = c_f/2$ and can be substituted for $d\theta/dx$ in (2.17). Thus, with $\partial\langle U\rangle^+/\partial x|_{y^+}$ expressed in terms of Π, θ, $s = \sqrt{2/c_f}$ and $(d/dx)\sqrt{c_f/2} = f(s, y_0, \Pi, I)$, the integration over y^+ required to evaluate term IV can be performed.

2.1.3. *Test on DNS data from smooth-wall turbulent boundary layers*

The present analysis and approximations described in the prior sections are used to evaluate the terms of (2.3), and the resulting profiles are compared with data from direct numerical simulation (DNS) of Sillero *et al.* (2013). This database provides
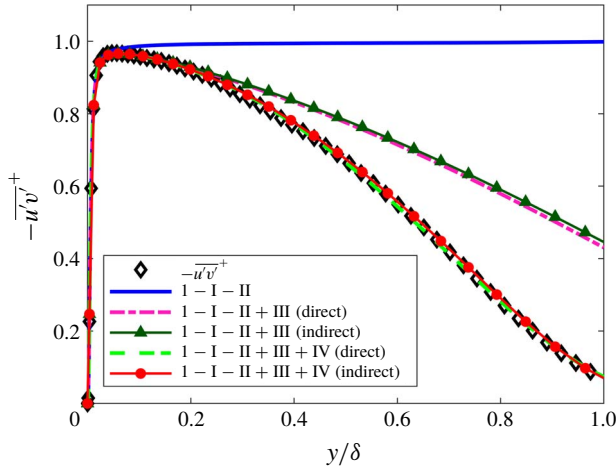
FIGURE 3. (Colour online) Terms of (2.3) as indicated in the legend for turbulent smooth-wall ZPG DNS of Sillero *et al.* (2013) at $Re_\theta = 6000$. Black diamonds ($\diamond$) are measured Reynolds shear stress. Dashed curves utilize directly calculated streamwise gradient terms. Solid curves with markers utilize the present method for indirectly calculating streamwise gradient terms.

detailed statistics for ZPG smooth-wall turbulent boundary layers from Re_θ of 4000 to 6500 in increments of 500. Figure 3 shows the terms of (2.3) calculated from the $Re_\theta = 6000$ profile statistics. The study's published u_τ was used to normalize all values. The Reynolds shear stress, $-\overline{u'v'}^+$, is the only non-zero term on the left-hand side of (2.3) since there was no spatial averaging required for this study. The left-hand side of (2.3) is plotted in the figure with black diamonds. The right-hand side terms of (2.3) which were calculated directly from multiple streamwise profiles are plotted in the figure with different dashed line styles. Profiles at Re_θ of 5500, 6000 and 6500 were used to calculate the streamwise gradients directly using a second-order accurate central difference numerical method at constant y^+. The right-hand side terms of (2.3), which were calculated indirectly using the present techniques described in this paper for a single streamwise profile, are plotted with solid lines with markers. Equation (2.13) requires κ and y_0 as parameters. $\kappa = 0.41$ and $A = 5.1$ were assumed, and $y_0 = (\nu/u_\tau)\mathrm{e}^{-\kappa A}$ was used as appropriate for a smooth wall.

Figure 3 shows the terms calculated with the two methods show excellent agreement with each other and the measured Reynolds shear stress data. Other pairs of κ and A found in the literature could have been selected and would have resulted in a small but observable difference in figure 3. $\kappa = 0.41$ and $A = 5.1$ were selected because they gave the best visual fit to the log-law region velocity data (not shown). This gives good confidence that the assumptions used to derive the indirect formulas for streamwise gradient terms were sound at least when applied to these data.

2.1.4. *Test on experimental data from smooth-wall turbulent boundary layers*

Next, the accuracy of the proposed approximations to the various terms in the momentum balance are tested on the smooth-wall ZPG experimental data of Morrill-Winter *et al.* (2015). The data set was acquired in the High Reynolds Number Boundary Layer Wind Tunnel (HRN-BLWT) at the University of Melbourne. The profiles shown in figure 4 are from $x = 11.9$ m with $U_e = 15.3$ m s^{-1}.
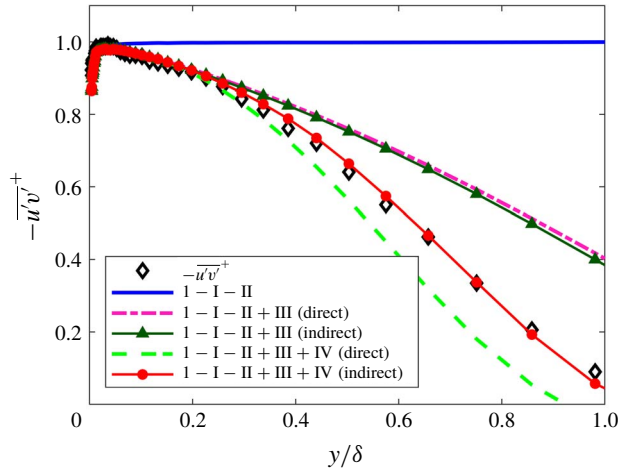
FIGURE 4. (Colour online) Terms of (2.3) as indicated in the legend for turbulent smooth-wall ZPG flow of Morrill-Winter *et al.* (2015) at $Re_\tau = 6080$. Black diamonds ($\diamondsuit$) are measured Reynolds shear stress. Dashed curves utilize directly calculated streamwise gradient terms. Solid curves with markers utilize the present method for indirectly calculating streamwise gradient terms.

Solid lines with markers show the present method. $\kappa = 0.384$ and $A = 4.17$ provided a close visual fit to the log-law region velocity data (not shown) and are common in papers from the HRN-BLWT. Terms I and II are the same as in Volino & Schultz (2018) and fit the measured Reynolds shear stress data very well through $y/\delta = 0.04$. Adding term III, the fit to the data is very good through $y/\delta = 0.2$. Adding term IV, both the direct and present methods fit the data well through $y/\delta = 0.3$. Above $y/\delta = 0.3$, the direct method slightly underestimates the shear stress while the present method shows good agreement to the measured shear stress data throughout the entire boundary layer.

2.1.5. *Test on experimental data from rough-wall turbulent boundary layers*

Figure 5 shows the direct and indirect methods of calculating (2.3) for data from Squire *et al.* (2016) with a ZPG turbulent boundary layer developing over a P36 grit sandpaper surface in the HRN-BLWT at the University of Melbourne. The profiles shown in figure 5 are from $x = 15$ m with $U_e = 17.4$ m s^{-1}. Both the direct and the present method fit the measured Reynolds shear stress data well through $y/\delta = 0.2$ with terms I, II and III included. The direct method maintains a good fit through the entire boundary layer when also including term IV. The present method overestimates the Reynolds shear stress above $y/\delta = 0.2$. This seems to be due to an underestimation of the friction velocity gradient magnitude in term III by (2.13). Red open circles show the result if term III is calculated assuming $\Pi = 0.55$ in (2.13) rather than calculating Π from (2.7) (as was suggested for some circumstances in § 2.1.1). A better fit to the data is observed with this assumption, and both the direct and present methods yield a close fit to the measured data through the entire boundary layer.

The overall very good agreement between total shear stress profiles determined using the proposed single profile approach and measured shear stress data confirms that the approach may be used to accurately estimate the friction velocity from profiles
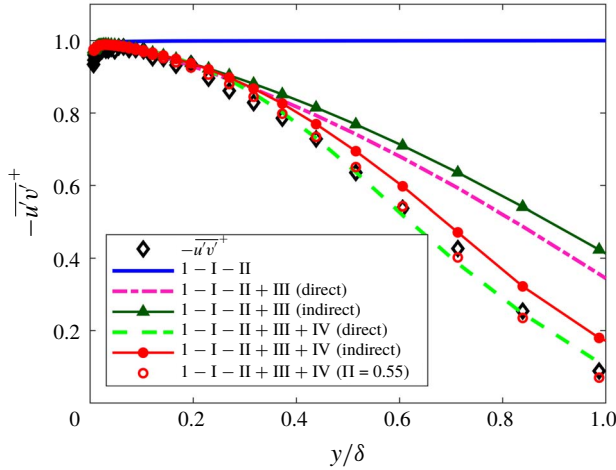
FIGURE 5. (Colour online) Terms of (2.3) as indicated in the legend for turbulent sand-grain surface ZPG flow of Squire *et al.* (2016) at $Re_\tau = 13\,140$. Black diamonds ($\diamondsuit$) are measured Reynolds shear stress. Dashed curves utilize directly calculated streamwise gradient terms. Solid curves with markers utilize the present method for indirectly calculating streamwise gradient terms. Red open circles ($\bigcirc$) utilize the present method and calculate term III assuming $\Pi = 0.55$ in (2.13).

at a single downstream position. It bears recalling that the essential assumption underlying the approach is a universal collapse of data as shown in figure 1 as well as some secondary assumptions, namely that W scales with δ and $\mathrm{d}\delta/\mathrm{d}\theta = \delta/\theta$ and that normal turbulent stress and $\partial\Pi/\partial x$ contributions are negligible.

2.2. *Determining roughness length and zero-plane displacement*

Rough walls add the need to determine the roughness length, y_0, and zero-plane displacement, d. As has been done by Placidi & Ganapathisubramani (2015) among others who have determined friction velocity independently, roughness length and zero-plane displacement can be determined by fitting the log-law equation (2.4) with measured mean streamwise velocity data in the log-law region. If a two-parameter fit of (2.4) is required, a convenient way to do this is to use a linear regression solver on a linear form of (2.4), $e^{\kappa U/u_\tau} = (1/y_0)y - d/y_0$. The left-hand side is known (or estimated if u_τ is unknown). If m and b are solutions for slope and intercept respectively, then $y_0 = 1/m$ and $d = -b/m$.

If y_0 or d is known or can be reasonably assumed, then a one-parameter fit to (2.4) may yield more accurate results. For example, Squire *et al.* (2016) assumed that d was at the midpoint of the sand-grain valleys and peaks and then performed a one-parameter fit for y_0.

It is also possible to use the log-law equation to determine y_0 for smooth-wall boundary layers and apply the present method to smooth surfaces. It should be noted that y_0 has no physical meaning for smooth walls. However, the relations presented prove useful in applying the present method to smooth walls. By assuming $d = 0$ and $\Delta U^+ = 0$ and equating (1.1) and (2.4), smooth-wall y_0 can be calculated by the explicit formula $y_0(u_\tau) = (\nu/u_\tau)e^{-\kappa A}$. As can be seen, smooth-wall y_0 is not constant since it is still dependent on u_τ.
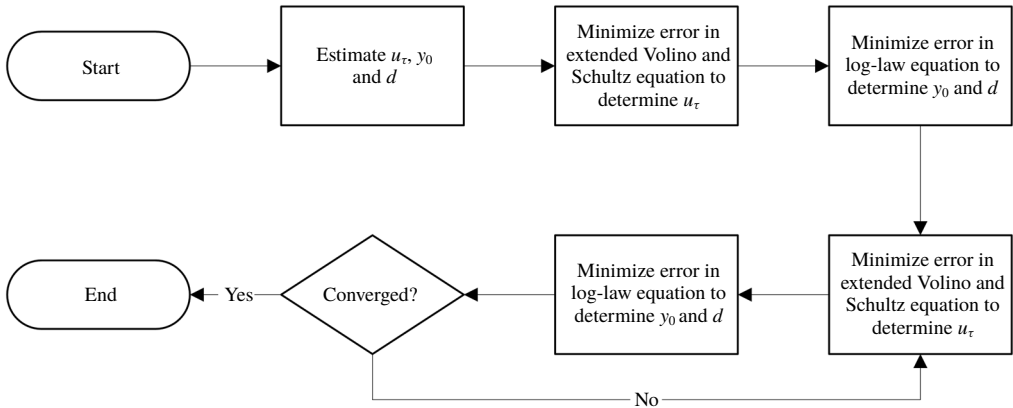
FIGURE 6. Flowchart of the iterative process for solving u_τ, y_0 and d. The extended Volino & Schultz equation refers to (2.3), and the log-law equation refers to (2.4).

2.3. *Practical implementation: iterative method*

When friction velocity is initially unknown, it may be determined through (2.3) and (2.4) through an iterative method. The process is illustrated in a flowchart in figure 6. An initial estimate of the friction velocity, roughness length and zero-plane displacement is required since both equations have dependencies in all three variables. Then, (2.3) is used to determine u_τ with the estimated y_0 and d by minimizing the error in (2.3) (note that u_τ enters in all of the terms) as explained in more detail when presenting applications below. Equation (2.3) is not highly sensitive to errors in y_0 and d, so determining u_τ with this equation first is the best way to reduce error in the initial estimate. However, since u_τ is determined only semi-independently from (2.3), iterations are required to refine the solution. Next, equation (2.4) is used to determine y_0 and d with the calculated u_τ from the previous step. Then, solution refinement proceeds iteratively between (2.3) and (2.4) until specified stopping criteria are met. The stopping criteria for the experimental data sets shown in § 3 were three significant digits for u_τ and y_0 or 10 iterations. Most data sets converged within a few iterations.

3. Applications to experimental data sets

In this section the analysis of terms in the momentum balance equation (which was presented in the prior section and led to the iterative method to determine the friction velocity based on single-location mean velocity and Reynolds shear stress profiles) is used to determine boundary layer parameters for various experimental data sets. Where required, κ and A were assumed to be 0.384 and 4.17, respectively, throughout § 3. The resulting friction velocities are compared to direct measurements using force balances or to prior published values.

3.1. *Boundary layers over rough sand-grain surfaces*

The comprehensive shear stress boundary layer analysis method was applied to the sand-grain boundary layer data from Squire *et al.* (2016). This study recorded detailed fluid profile statistics with a cross-wire anemometry probe at multiple Reynolds numbers. The study also utilized a drag balance for independently measuring friction velocity directly at three of the Reynolds numbers tested. The present method is
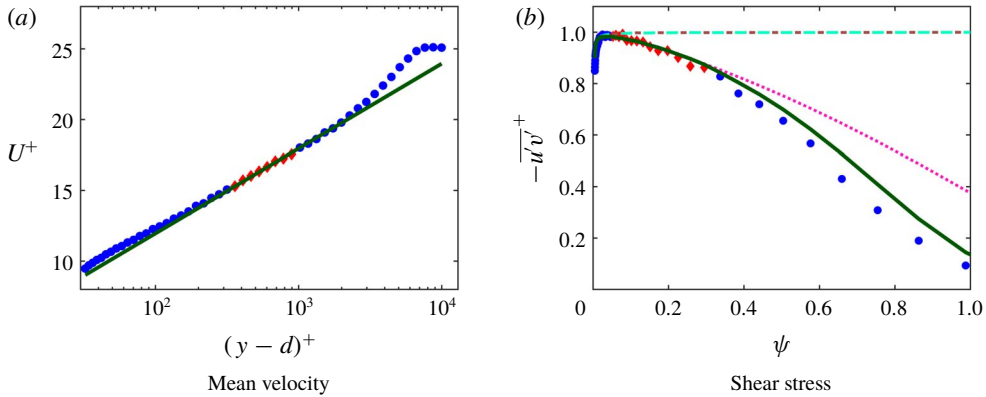
FIGURE 7. (Colour online) Comparison of data and fits from the proposed method for mean velocity (*a*) and shear stress (*b*) profiles from Squire *et al.* (2016) at $Re_\tau = 6770$. Blue circles (●) are measured data, and red diamonds (◆) are fitted data. Fit to (2.4) performed on data between $0.07 < \psi_{(k)} < 0.15$, and fit to (2.3) performed on data between $0.05 < \psi_{(k)} < 0.30$. Green lines show (2.4) in (*a*) and (2.3) in (*b*). Dotted or dashed line styles show components of (2.3): brown dash-dot line is $1 - \mathrm{I}$, cyan dashed line is $1 - \mathrm{I} - \mathrm{II}$ and magenta dotted line is $1 - \mathrm{I} - \mathrm{II} + \mathrm{III}$.

used to analyse turbulent boundary layer data with only the fluid measurements and without the friction velocity data from the force balance at the three Reynolds numbers profiled above the drag balance location. Figure 7 shows the present method's result for the sand-grain surface with $Re_\tau = 6770$. Figure 7(*a*) shows the mean streamwise velocity profile versus wall-normal distance, and figure 7(*b*) shows the Reynolds shear stress data versus wall-normal distance, in inner and outer scaling, respectively. The outer-scaled wall-normal distance, ψ, is calculated by

$$\psi = \frac{y - d}{\delta - d}. \tag{3.1}$$

Evidence from Volino & Schultz (2018) showed that reasonable estimates of flow below the nearest velocity data to the wall can be used to improve results. The estimated velocities only affect the integral terms in (2.3). In the following results, a cubic interpolation is used to estimate mean streamwise velocity between the nearest data point and an assumed zero velocity at $y = d$. Flow below $y = d$ is assumed to be a negligible portion of the integrals, which is consistent with evidence from Volino & Schultz (2018). This is not proposed as a universal method for interpolation but works well for better estimating the integral terms of (2.3).

Having presented the results from the method as applied to the data, some details about the iterative procedure are presented next. Initial estimates for u_τ, y_0 and d may be used with (2.3) and (2.4) to start the iterative process shown in figure 6 for solving the unknowns. To illustrate the process, root mean square (r.m.s.) error plots in the variable parameter space are shown in figure 8. The r.m.s. error for (2.3) is calculated as usual according to

$$\text{r.m.s. error} = \sqrt{\frac{1}{n} \sum_{k=1}^{n} [-\langle \overline{u'v'} \rangle_{(k)}^+ - \langle \tilde{u}\tilde{v} \rangle_{(k)}^+ - (1 - \mathrm{I} - \mathrm{II} + \mathrm{III} + \mathrm{IV})_{(k)}]^2}, \tag{3.2}$$
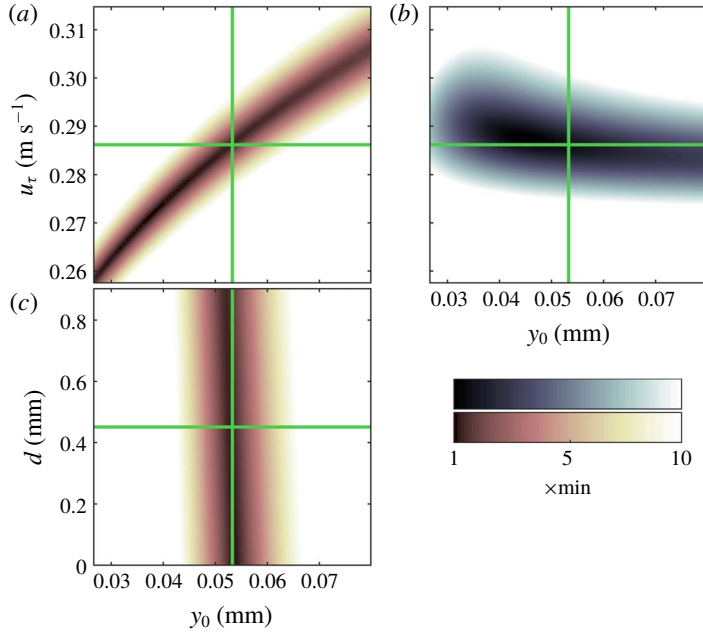
FIGURE 8. (Colour online) Contour plots of r.m.s. errors of fits to experimental data for boundary layer flow over sand-grain surface at $Re_\tau = 6770$ from Squire *et al.* (2016). Panels (*a,c*) show the mean velocity r.m.s. errors between (2.4) and experimental data in the range $0.07 < \psi_{(k)} < 0.15$ calculated as shown in (3.3). Panel (*b*) shows the r.m.s. error between (2.3) and experimental data in the range $0.05 < \psi_{(k)} < 0.30$ calculated as shown in (3.2). The green lines show the converged values for u_τ, y_0 and d on the plots.

where the summation is over the *n* experimental data points between $0.05 < \psi_{(k)} < 0.30$. Figure 8(*b*) shows the r.m.s. error in the u_τ–y_0 plane and indicates that the r.m.s. error is much more sensitive to changes in u_τ than changes in y_0 in the fitted region. The process of solving (2.3) for u_τ effectively solves for the minimum on a vertical line of this plot since y_0 is assumed as given in this step of the process. This plot also helps illustrate that the error minimization from the comprehensive shear stress profile is well suited for solving u_τ accurately.

Figure 8(*a,c*) shows r.m.s. error for (2.4) for the experimental data between $0.07 < \psi_{(k)} < 0.15$ calculated by

$$\text{r.m.s. error} = \sqrt{\frac{1}{n} \sum_{k=1}^{n} \left[\frac{\langle U(y_{(k)}) \rangle}{u_\tau} - \frac{1}{\kappa} \ln \left(\frac{y_{(k)} - d}{y_0} \right) \right]^2}. \tag{3.3}$$

Figure 8(*c*) is the r.m.s. error in the d–y_0 plane which is the solution plane of interest for this step in the process. The range of d on the vertical axis encompasses the total height of the sand-grain roughness from valleys to peaks. This is the total possible range for d in accordance with the physical definition proposed by Jackson (1981). The plot shows a strong dependence on y_0 but very weak dependence on d in this range. For some experimental data sets including this case, a two-parameter fit of (2.4) can result in non-physical values of d which should fall between the peaks and valleys of the roughness. Therefore, in some cases it may be more advantageous to

Re_τ	Drag balance (m s^{-1})	Present method (m s^{-1})	% difference
6770	0.288	0.286	−0.47
12 300	0.488	0.490	0.41
17 190	0.698	0.693	−0.67

TABLE 1. Squire *et al.* (2016) published drag balance friction velocity and the present method's calculated friction velocity by fitting data between $0.05 < \psi_{(k)} < 0.30$ to (2.3) and fitting data between $0.07 < \psi_{(k)} < 0.15$ to (2.4).

assume a reasonable *d*. For the case of figure 7 and the other two cases in table 1, *d* was assumed to be the midpoint between peaks and valleys of the sand-grain surface as was assumed by Squire *et al.* (2016) and Morrill-Winter *et al.* (2017). Then a numerical solver was used to minimize (3.3) with y_0 only, which solves for the minimum error on a horizontal line of figure 8(*c*) rather than the absolute minimum error as a two-parameter fit would.

Iteration between solving (2.3) for u_τ and solving (2.4) for y_0 converges to a unique solution because of the different sensitivities in the u_τ–y_0 plane shown in figure 8(*a,b*). Iteration progresses until the process converges to a unique solution. The green lines show the converged values for u_τ, y_0 and *d* for the case of figure 7.

Table 1 contains the three cases from Squire *et al.* (2016) where fluid profiles were measured directly over the HRN-BLWT drag balance. Table 1 shows that the results from the present method of determining friction velocity agree with the direct drag balance measurements within $\pm 1\%$. This agreement is well within the experimental uncertainties and shows the present method to be a reliable analysis technique when only fluid dynamic measurements are available at a single streamwise location.

3.2. *Boundary layers over smooth walls*

Next, the present method is applied to the smooth-wall fluid profile data from Morrill-Winter *et al.* (2015). Determining y_0 and *d* from the log-law equation, (2.4), in the flowchart of figure 6 is replaced with the explicit formula $y_0(u_\tau) = (\nu/u_\tau)\mathrm{e}^{-\kappa A}$ and with $d = 0$ as described in §2.2. Figure 9 shows fits of (2.3) and (2.4) for the smooth-wall ZPG flow at $Re_\tau = 1951$.

Table 2 shows friction velocity results for a range of Reynolds numbers from the HRN-BLWT smooth-wall cases. The present method calculates u_τ within $\pm 1\%$ of the published values from a single profile of fluid dynamic measurements for all cases analysed. While this study did not utilize a drag balance for friction velocity, Morrill-Winter *et al.* (2015) used the composite fit method from Chauhan, Monkewitz & Nagib (2009) which has been validated extensively. The very good agreement of results in figure 9 and table 2 again show the present method to be a very accurate analysis technique and the indirect methods for calculating streamwise gradients in (2.3) to be reliable.

3.3. *Boundary layers over arrays of wall attached staggered cubes*

The present method is also demonstrated for boundary layer data from Cheng & Castro (2002) for flow over an array of wall attached cubes. Cross-wire anemometry profiles were recorded at multiple locations over a repeating unit for five different cases. Spatially averaged profiles from the 20 mm staggered cube array with 25 %
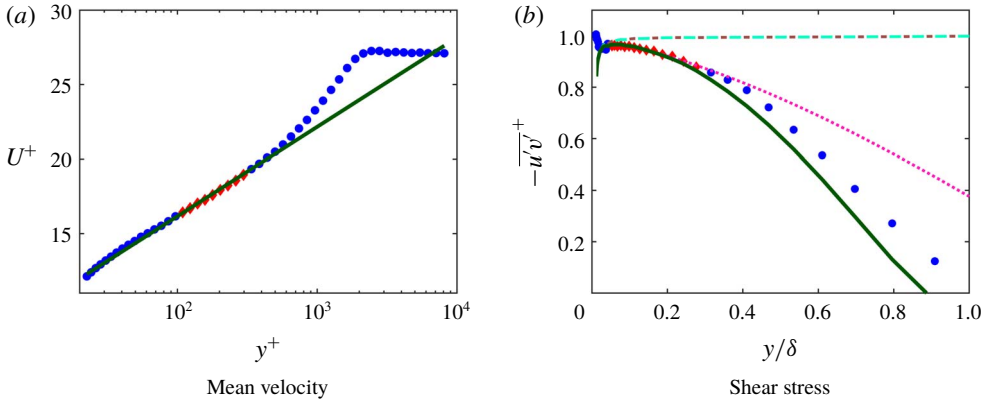
FIGURE 9. (Colour online) Comparison of data and fits from the proposed method for mean velocity (*a*) and shear stress (*b*) profiles from Morrill-Winter *et al.* (2015) at $Re_\tau = 1951$. Blue circles (●) are measured data, and red diamonds (◆) are fitted data. Fit to (2.4) performed on data between $0.07 < y_{(k)}/\delta < 0.15$, and fit to (2.3) performed on data between $0.05 < y_{(k)}/\delta < 0.30$. Green lines show (2.4) in (*a*) and (2.3) in (*b*). Dotted or dashed line styles show components of (2.3): brown dash-dot line is $1 - I$, cyan dashed line is $1 - I - II$ and magenta dotted line is $1 - I - II + III$.

Re_τ	Published value (m s^{-1})	Present method (m s^{-1})	% difference
1951	0.368	0.370	0.53
2622	0.356	0.357	0.22
2928	0.541	0.543	0.41
3770	0.519	0.517	−0.40
3844	0.340	0.341	0.16
5593	0.334	0.336	0.55
6080	0.512	0.510	−0.39
7894	0.497	0.497	0.04

TABLE 2. Morrill-Winter *et al.* (2015) published friction velocities and the present method's calculated friction velocities by fitting data between $0.05 < y_{(k)}/\delta < 0.30$ to (2.3) and fitting data between $0.07 < y_{(k)}/\delta < 0.15$ to (2.4).

planform surface density are shown here in figure 10 with fits from (2.3) and (2.4). Since the profiles shown are spatially averaged, the dispersive shear stress term is non-zero and included although it is small enough to be considered negligible. The r.m.s. error plots for these fits are shown in figure 11. Equation (2.4) is fit for data between $0 < \psi_{(k)} < 0.22$ which is equivalent to the published range used for this fit by Cheng & Castro (2002). Equation (2.3) was fit between $0.15 < \psi_{(k)} < 0.30$. Additionally, this test case had a single 20 mm brass cube which was instrumented with 21 pressure taps on the windward and leeward sides of the cube to directly measure pressure drag. In the fully rough regime, the pressure drag is very nearly the total surface drag. The same geometry was also tested in Cheng *et al.* (2007) with both the pressure-tapped cube and a floating element drag balance which will allow additional comparison for the friction velocity results.

As is evident from the results in table 3, the present comprehensive shear stress method does not seem any better than earlier approaches. The difference between the
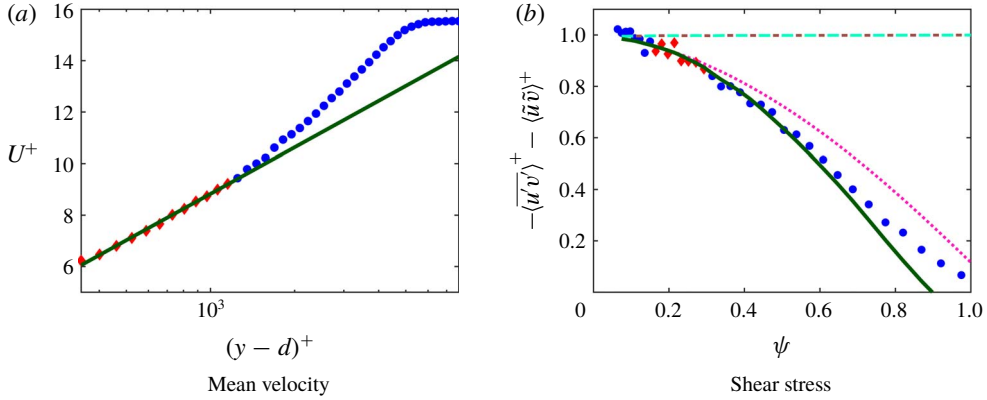
FIGURE 10. (Colour online) Comparison of data and fits from the proposed method for mean velocity (*a*) and shear stress (*b*) profiles from Cheng & Castro (2002) for flow over staggered 20 mm cubes. Blue circles (●) are measured data, and red diamonds (◆) are fitted data. Fit to (2.4) performed on data between $0 < \psi_{(k)} < 0.22$, and fit to (2.3) performed on data between $0.15 < \psi_{(k)} < 0.30$. Green lines show (2.4) in (*a*) and (2.3) in (*b*). Dotted or dashed line styles show components of (2.3): brown dash-dot line is $1 - \mathrm{I}$, cyan dashed line is $1 - \mathrm{I} - \mathrm{II}$ and magenta dotted line is $1 - \mathrm{I} - \mathrm{II} + \mathrm{III}$.
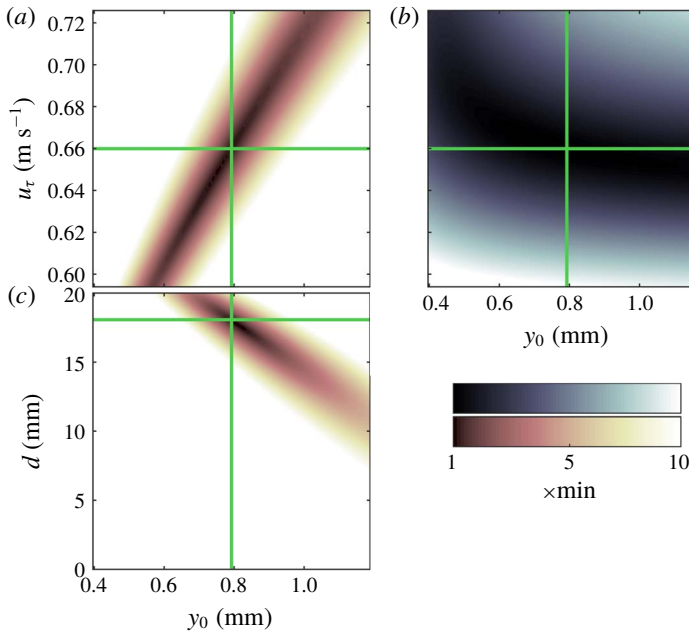
FIGURE 11. (Colour online) Contour plots of r.m.s. errors of fits to experimental data for boundary layer flow over staggered cubes from Cheng & Castro (2002). Panels (*a,c*) show the mean velocity r.m.s. errors between (2.4) and experimental data in the range $0 < \psi_{(k)} < 0.22$ calculated as shown in (3.3). Panel (*b*) shows the r.m.s. error between (2.3) and experimental data in the range $0.15 < \psi_{(k)} < 0.30$ calculated as shown in (3.2). The green lines show the converged values for u_τ, y_0 and d on the plots.

Friction velocity method	$\dfrac{u_\tau}{U_e}$	% difference from PT	% difference from FE
Pressure-tapped cube form drag (PT)	0.0718	0.0	1.5
Floating element drag balance (FE)	0.0707	-1.5	0.0
Published traditional total shear stress	0.0640	-10.9	-9.6
Comprehensive shear stress (present)	0.0644	-10.3	-8.9

TABLE 3. Differences between published friction velocities and the present method's calculated friction velocity assuming ZPG. Hot-wire profiles for the present method were from Cheng & Castro (2002). Published friction velocities are from Cheng *et al.* (2007).

present method and the direct measures is still approximately 8 %–11 %. Additionally, even though (2.3) seems to fit the shear stress data below $\psi < 0.5$ in figure 10(*b*), there are visual discrepancies in the slope particularly in the near-wall region, $\psi < 0.25$, where the equation should be the most accurate (due to less experimental error in the integral terms). This difference tends to lower the fitted value of friction velocity in agreement with other fluids based methods and no closer to the direct measurements.

The key problem with the results in table 3 is the discrepancy between the direct measurement methods and total shear stress methods (including the present method as applied above). In study after study, the traditional total shear stress methods seem to under-predict the friction velocity which has resulted in considerable discussion in the literature, such as in Cheng *et al.* (2007), Claus, Krogstad & Castro (2012) and Ferreira *et al.* (2018). The discussions persist to this date because, to the authors' knowledge, this empirical discrepancy has not been quantified by physical equations. Additionally, studies by Reynolds & Castro (2008) and Placidi & Ganapathisubramani (2015) both cite Cheng & Castro (2002) and Cheng *et al.* (2007) for evidence-based corrections to the friction velocity which they determine from traditional total shear stress methods.

One of the possibilities noted by Cheng *et al.* (2007) and Ferreira *et al.* (2018) is that a small favourable pressure gradient (FPG) may cause this effect on the Reynolds shear stress. The University of Surrey and University of Southampton tunnels where these studies were conducted are considered nominally zero pressure gradient. However, both tunnels have a fixed cross-sectional area which imposes a small favourable pressure gradient due to boundary layer growth. From reported boundary layer growth in Cheng *et al.* (2007) and the tunnel dimensions, it can be estimated that the acceleration parameter was approximately $K = 2 \times 10^{-8}$. This acceleration parameter is small (but non-zero) and in the range of values from the similarly sized fixed cross-section tunnel in Placidi & Ganapathisubramani (2019).

Therefore, in evaluating term IV, $d\theta/dx$ may be replaced with the full MIE shown by

$$\frac{d\theta}{dx} = \frac{c_f}{2} - \left(\frac{2\theta}{\delta} + \frac{\delta^*}{\delta} \right) \left(\frac{U_e \delta}{\nu} \right) K \tag{3.4}$$

to solve $\partial \langle U \rangle^+ / \partial x |_{y^+}$ from (2.17). Also, for term III of (2.3), equation (2.13) may still be used to solve $(d/dx)\sqrt{c_f/2}$. The evidence from Castro (2007) indicates that (2.13) still holds for small FPG boundary layers. Castro (2007) shows a plot of c_f versus $(x - x_0)/y_0$. Equation (2.13) is derived from the curve in Castro's plot, and most (if
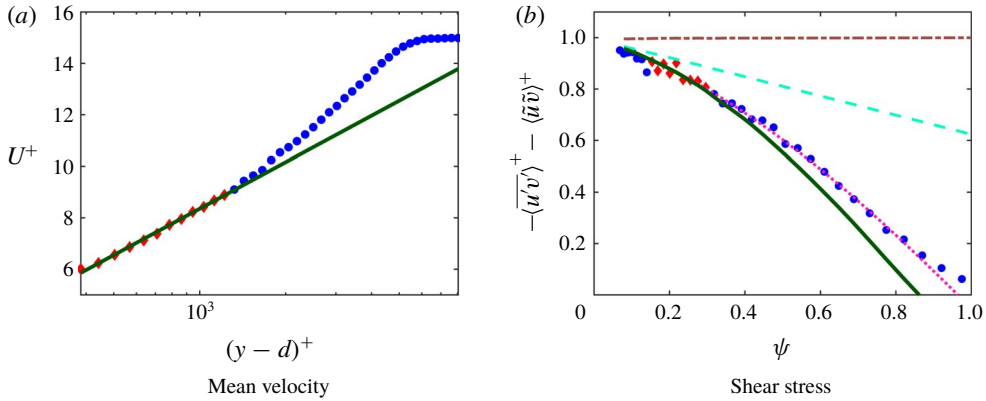
FIGURE 12. (Colour online) Comparison of data and fits from the proposed method for mean velocity (*a*) and shear stress (*b*) profiles from Cheng & Castro (2002) for flow over staggered 20 mm cubes. Blue circles (●) are measured data, and red diamonds (◆) are fitted data. Fit to (2.4) performed on data between $0 < \psi_{(k)} < 0.22$, and fit to (2.3) performed on data between $0.15 < \psi_{(k)} < 0.30$. Green lines show (2.4) in (*a*) and (2.3) in (*b*). Dotted or dashed line styles show components of (2.3): brown dash-dot line is $1 - I$, cyan dashed line is $1 - I - II$ and magenta dotted line is $1 - I - II + III$. Equation (2.3) is calculated assuming a small FPG with $K = 2 \times 10^{-8}$.

Friction velocity method	$\dfrac{u_\tau}{U_e}$	% difference from PT	% difference from FE
Pressure-tapped cube form drag	0.0718	0.0	1.5
Floating element drag balance	0.0707	−1.5	0.0
Published traditional total shear stress	0.0640	−10.9	−9.6
Comprehensive shear stress (present)	0.0668	−7.0	−5.6

TABLE 4. Differences between published friction velocities and the present method's calculated friction velocity assuming small FPG with $K = 2 \times 10^{-8}$. Hot-wire profiles for the present method were from Cheng & Castro (2002). Published friction velocities are from Cheng *et al.* (2007).

not all) of the experimental data on the plot are from fixed cross-section tunnels with small FPGs.

Figure 12 shows Cheng & Castro (2002) cross-wire anemometry data with fits from (2.3) and (2.4) using the present method. Equation (2.3) is now calculated for a small FPG which assumes $K = 2 \times 10^{-8}$. Equation (2.3) now agrees with the turbulent shear stress data well through $\psi < 0.4$. Furthermore, it matches the slope below $\psi < 0.25$ where it had not previously. Comparing figures 10(*b*) and 12(*b*), the effect on the terms of (2.3) is readily seen. Term II, a purely pressure dependent term, was zero in figure 10 but approximately half of the total shear stress throughout the boundary layer in figure 12. Additionally, the magnitude of both terms III and IV were reduced due to the positive K in term III and (3.4). The overall effect from the pressure gradient flattened the turbulent shear stress profile throughout the boundary layer by reducing the inertial terms and increasing the pressure-dependent terms.

Table 4 compares results from the present method now assuming a small favourable pressure gradient. The present result is now 7 % lower than the pressure-tapped cube
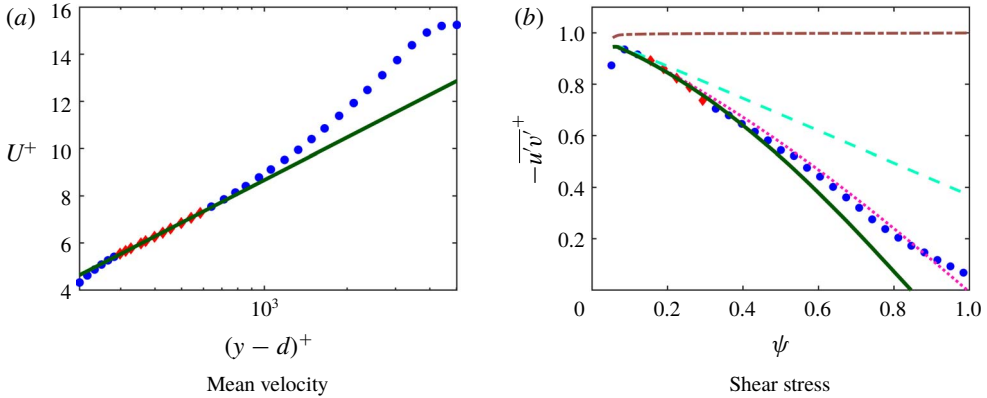
FIGURE 13. (Colour online) Comparison of data and fits from the proposed method for mean velocity (*a*) and shear stress (*b*) profiles from Placidi & Ganapathisubramani (2015) LEGO® block geometry LP2 at $Re_\tau = 7642$. Blue circles (●) are measured data, and red diamonds (◆) are fitted data. Some data points were removed for clarity. Fit to (2.4) performed on data between $0.07 < \psi_{(k)} < 0.15$, and fit to (2.3) performed on data between $0.15 < \psi_{(k)} < 0.30$. Green lines show (2.4) in (*a*) and (2.3) in (*b*). Dotted or dashed line styles show components of (2.3): brown dash-dot line is $1 - I$, cyan dashed line is $1 - I - II$ and magenta dotted line is $1 - I - II + III$. Equation (2.3) is calculated with K from table 5.

and 6 % lower than the floating element drag balance. This is encouraging because the comprehensive shear stress method is now within the 10 % published uncertainty of the pressure-tapped cube measurements in Cheng *et al.* (2007). The floating element drag balance does not appear to have published information regarding experimental uncertainty. It may be assumed that the uncertainty is at least 3 % which would be in line with other floating element drag balances used in a similar tunnel by Placidi & Ganapathisubramani (2015) and Ferreira *et al.* (2018). Additionally, the uncertainty in the present method is unknown especially given that K was estimated with limited information. Given these uncertainties the present method appears to be an improvement to prior single fluid profile measurement approaches.

3.4. *Boundary layers over arrays of LEGO® blocks*

Placidi & Ganapathisubramani (2015, 2018) tested 12 fully rough surfaces with different repeating patterns of LEGO® blocks. The studies were nominally zero pressure gradient and reported that $K < 5 \times 10^{-8}$. The authors published the data set online in Placidi & Ganapathisubramani (2019) which included calculated pressure gradients. The study published u_τ values from direct measurement with a force balance, and y_0 and d were found with a least square regression of the log-law equation using the friction velocity measured from the force balance. The drag balance in this study was based on the design documented in Krogstad & Efros (2010) and is expected to be more accurate than the one in Cheng *et al.* (2007).

Turbulent boundary layer data plotted in figure 13 were recorded by particle image velocimetry over the surface geometry named LP2 at $Re_\tau = 7642$. Figure 13 shows fits to the particle image velocimetry data for (2.3) and (2.4). Placidi & Ganapathisubramani (2019) published $K = 4.3 \times 10^{-8}$ for this case. Equation (2.4) was fitted to velocity data between $0.07 < \psi_{(k)} < 0.15$ in figure 13(*a*), and (2.3) was fitted to shear stress data between $0.15 < \psi_{(k)} < 0.30$ in figure 13(*b*).

Case	Drag balance (m s^{-1})	Present method assuming ZPG (m s^{-1})	% difference (ZPG)	Present method assuming FPG (m s^{-1})	% difference (FPG)	$K \times 10^{-8}$
LP1	0.81	0.81	−0.4	0.82	1.3	1.2
LP2	0.78	0.72	−7.9	0.77	−1.8	4.3
LP3	0.71	0.68	−3.9	0.71	−0.1	2.9
LP4	0.67	0.65	−2.8	0.69	3.7	4.3
LP5	0.66	0.62	−5.9	0.66	0.3	4.2
LP6	0.67	0.55	−18.4	0.56	−16.8	1.2

TABLE 5. Differences between Placidi & Ganapathisubramani (2015) published drag balance friction velocity and the present method's calculated friction velocities by fitting data between $0.15 < \psi_{(k)} < 0.30$ to (2.3) and fitting data between $0.07 < \psi_{(k)} < 0.15$ to (2.4). Acceleration parameters, K, obtained from Placidi & Ganapathisubramani (2019).

All six surfaces from Placidi & Ganapathisubramani (2015) with constant frontal density (LP1–LP6) were analysed with the present method assuming both a ZPG and a small FPG. In some cases, it was necessary to fix the range of possible d to within the roughness height due to the physical interpretation of d described in Jackson (1981). Placidi & Ganapathisubramani (2015) also noted this was necessary for some cases in their analysis. Results are included in table 5. The present method's result was consistently lower than the drag balance measurement when a ZPG was assumed but was close to the experimental uncertainty of the drag balance for five of the six cases when the reported K (for the small FPG) was utilized. Case LP6, which differed by −18 % or −17 %, remains as an outlier for which the present fluid dynamic measurements alone do not agree with the drag balance measurement.

Placidi & Ganapathisubramani (2015) reported that it was necessary to increase u_τ determined from traditional total shear stress methods by 12 % in order to obtain agreement within 5 % of the drag balance results for all cases. The present method does not need a correction factor and achieves considerably better results both assuming a ZPG and small FPG. Utilizing the reported K for the small FPG leads to results that are near the uncertainty of the study's drag balance in a tunnel similar to the one in Cheng & Castro (2002). These results give strong evidence that the small FPG explains the often cited friction velocity discrepancy from Cheng & Castro (2002).

3.5. *Friction velocity sensitivity*

The comprehensive shear stress method assumes κ, the fitting range for the extended Volino & Schultz equation, (2.3), and the fitting range for the log-law equation, (2.4), when solving for u_τ, y_0 and d. A trivariate sensitivity analysis was performed on surface geometry LP2 from Placidi & Ganapathisubramani (2015). Converged values of u_τ, y_0 and d were calculated for all 150 combinations of κ, fitting range to (2.3), and fitting range to (2.4) from table 6. Figure 15 shows scatter plots of the results projected onto the three planes created by u_τ, y_0, and d. Friction velocity results show low sensitivity to the assumed parameters with u_τ bounded within ±2 % of the results from §3.4.

While friction velocity showed low sensitivity, results for y_0 ranged from 38 % below to 5 % above the results from §3.4. Also, results for d included nearly the entire upper 1/3 of the roughness height. The variances in y_0 and d were primarily
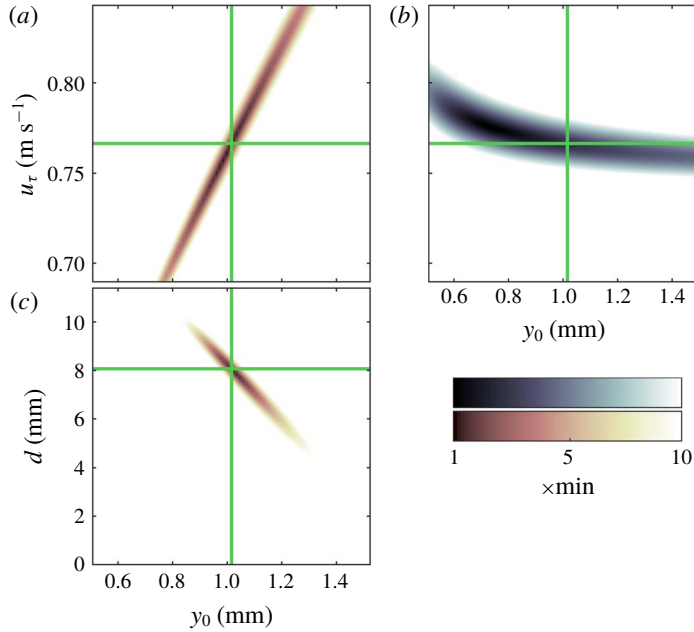
FIGURE 14. (Colour online) Contour plots of r.m.s. errors of fits to experimental data for boundary layer flow from Placidi & Ganapathisubramani (2015) LEGO® block geometry LP2. Panels (*a,c*) show the mean velocity r.m.s. errors between (2.4) and experimental data in the range $0.07 < \psi_{(k)} < 0.15$ calculated as shown in (3.3). Panel (*b*) shows the r.m.s. error between (2.3) and experimental data in the range $0.15 < \psi_{(k)} < 0.30$ calculated as shown in (3.2). The green lines show the converged values for u_τ, y_0 and d on the plots.

κ	Fitting range for (2.3)	Fitting range for (2.4)
0.38	$0.10 < \psi_{(k)} < 0.25$	$0.00 < \psi_{(k)} < 0.15$
[0.384]	$0.15 < \psi_{(k)} < 0.25$	$[0.07 < \psi_{(k)} < 0.15]$
0.39	$0.10 < \psi_{(k)} < 0.30$	$0.10 < \psi_{(k)} < 0.15$
0.40	$[0.15 < \psi_{(k)} < 0.30]$	$0.00 < \psi_{(k)} < 0.19$
0.41	$0.20 < \psi_{(k)} < 0.30$	$0.07 < \psi_{(k)} < 0.19$
		$0.10 < \psi_{(k)} < 0.19$

TABLE 6. Parameter variations for univariate and trivariate sensitivity analysis for Placidi & Ganapathisubramani (2015). Bracketed parameters indicate the initial assumptions from §3.4.

from the high sensitivity inherent in fitting the log-law equation, equation (2.4). The present method shares this limitation with other methods that rely on two-parameter fits to the log-law equation. However, the selected log-law fitting range does not greatly affect the friction velocity result.

A univariate analysis was also performed for all cases with constant frontal density from Placidi & Ganapathisubramani (2015) excluding the outlier, LP6. In each plot of figure 16, one of the three assumed parameters was allowed to vary with the values listed in table 6 while maintaining the initial assumptions from §3.4 in the other two parameters. The varying parameter is labelled on the horizontal axis with the
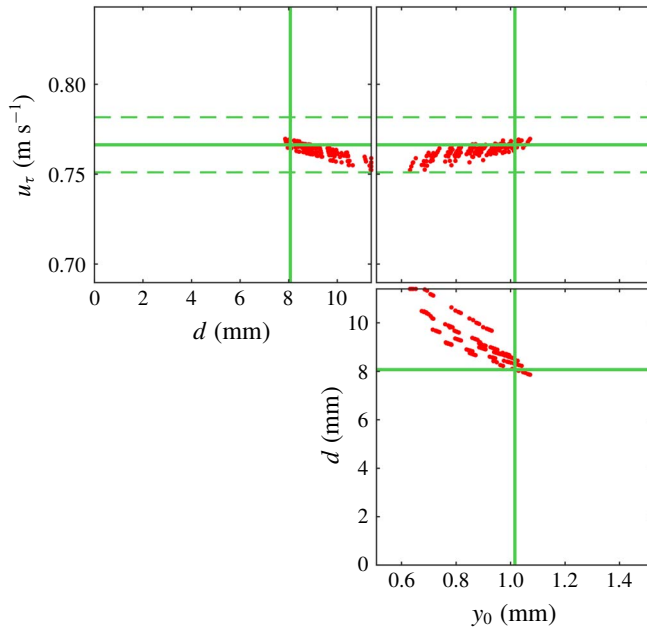
FIGURE 15. (Colour online) Scatter plots showing u_τ, y_0 and d trivariate sensitivity to assumptions of κ, fitting range for (2.3), and fitting range for (2.4) applied to data from Placidi & Ganapathisubramani (2015) LEGO® block geometry LP2. The solid green lines show the converged values plotted in figure 14. The dashed green lines show $u_\tau \pm 2\%$.
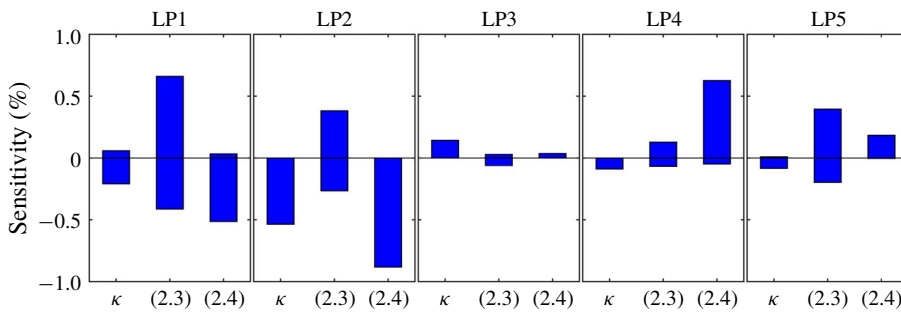

FIGURE 16. (Colour online) Bar plots showing univariate sensitivity of u_τ to assumptions of κ, fitting range for (2.3), and fitting range for (2.4) applied to data from Placidi & Ganapathisubramani (2015). Per cent sensitivity bars show the maximum positive and negative per cent differences to the u_τ reported in table 5 for each case.

vertical axis showing the maximum positive and negative per cent difference to the u_τ reported in table 5 for each case. The figure shows that each of the three assumptions individually affect the friction velocity result by less than $\pm 1\%$.

4. Summary

4.1. *Key assumptions*

Several key assumptions were included in the derivation and application of the present method and are reviewed here. First, simplification of the integral form of the
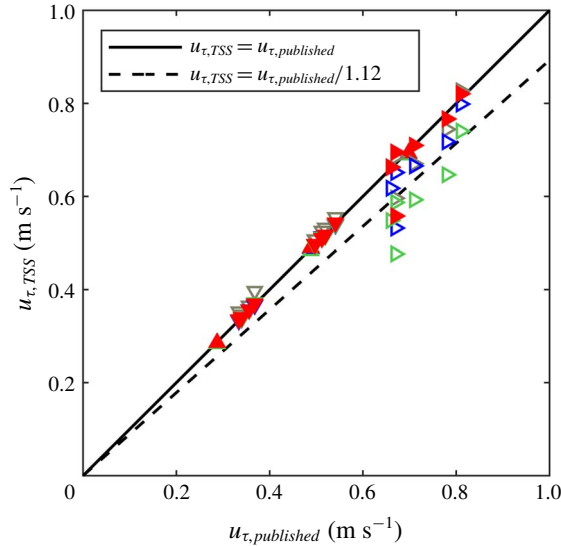
FIGURE 17. (Colour online) Friction velocities determined using different total shear stress (TSS) approaches, plotted against published friction velocities. Filled red symbols utilize the present comprehensive shear stress method. Open blue symbols utilize total shear stress points in the plateau region. Open green symbols utilize total shear stress points in the roughness sublayer and inertial sublayer (RS+IS). Open grey symbols utilize the peak total shear stress. Up triangle (▲) data are from Squire *et al.* (2016). Down triangle (▼) data are from Morrill-Winter *et al.* (2015). Right triangle (►) data are from Placidi & Ganapathisubramani (2015).

Reynolds-averaged and spatially averaged streamwise momentum equation assumed that Reynolds normal stresses were negligible and the flow was two-dimensional. Second, the derivation assumed that the skin friction law, equation (2.10), was applicable. There were several assumptions embedded in the skin friction law which were discussed in § 2.1.1, but the skin friction law was shown to have robust applicability both in § 2.1.1 and Castro (2007). Third, the friction velocity gradient equation, (2.13), used the ZPG MIE. However, it was noted that Castro (2007) applied the ZPG MIE to nominally ZPG boundary layers with good agreement. Also, results from § 3 imply that this was a valid assumption for $K \lesssim 5 \times 10^{-8}$. Fourth, the velocity gradient profile derivation assumed that velocity profiles would collapse in outer scaling over a streamwise distance. This condition implies that $\partial \Pi / \partial x \approx 0$, W scales with δ and $\partial \delta / \partial \theta \approx \delta / \theta$ and is also sensitive to pressure gradient (and probably other parameters). However, the velocity gradient profile only appears in term IV of (2.3) which was not significant for $\psi < 0.3$ in most cases. Thus, it can be more easily avoided by choosing an appropriate fitting range.

4.2. *Results and comparisons with other methods*

Figure 17 compares published measured friction velocity for rough-wall cases and the published composite fit friction velocity for smooth cases to traditional total shear stress methods and to the present method. Red points for the present method fall close to the 45° line indicating excellent agreement with the published friction velocities. The one outlier is from surface LP6 from Placidi & Ganapathisubramani

(2015) as discussed in §3.4. It is noted that no other method provided results within 11 % of the measured friction velocity for this case. Other approaches are shown on the figure with blue, green and grey open symbols, showing larger scatter and a downward bias. The dotted line shows the total shear stress friction velocity for which a 12 % correction would equal the drag balance friction velocity. It can be seen why it may be appropriate to utilize the 12 % empirical correction for some cases from Placidi & Ganapathisubramani (2015) utilizing all total shear stress data from the roughness sublayer and inertial sublayer. However, other methods utilizing the plateau in the total shear stress and peak total shear stress provided results closer to the solid line. All total shear stress methods performed comparably for the smooth- and rough-wall cases from Morrill-Winter *et al.* (2015) and Squire *et al.* (2016), respectively.

Overall, no other total shear stress method performed as consistently well as the present method across all data sets considered. Besides one outlier, all cases utilizing the present method were within ±4 % of the friction velocity measured with a drag balance.

5. Conclusions

A detailed analysis of several terms entering in the mean momentum balance of turbulent boundary layers was performed. The results were useful in formulating a new comprehensive shear stress method for determining friction velocity. The approach is based on measured profiles of mean velocity and turbulent shear stress at a single downstream location and can be used for analysing nominally zero pressure gradient turbulent boundary layers. The approach extends an equation from Volino & Schultz (2018) to include spatial averaging and to calculate streamwise gradients from a single streamwise location. Two key elements are necessary to indirectly calculate streamwise gradients from a single two-component velocity profile. The first key element is the replacement of the streamwise gradient of friction velocity with an assumption of the skin friction law and momentum integral equation. The second key element is the assumption that the wake function scales with boundary layer thickness and can be connected to the streamwise gradient through the momentum integral equation. Application of the extended Volino & Schultz equation to various data sets showed the equation models turbulent shear stress data throughout the boundary layer. An iterative procedure combining fitting of the extended Volino & Schultz equation to the turbulent shear stress profile and fitting of the log-law equation to the mean velocity profile was proposed and implemented. Applications to various flows illustrated that the proposed method achieves similar friction velocity results as force balance measurements but only requires mean velocity and turbulent shear stress profiles. Results also demonstrated that even small pressure gradients, which can arise in fixed cross-section facilities, can have a significant (and often neglected) effect on turbulent shear stresses and may account for 10 % or more in friction velocity discrepancy with force balance measurements. The comprehensive shear stress method presented can account for this discrepancy in nominally zero pressure gradient facilities, leading to improved accuracy when determining friction velocity and skin friction drag in boundary layer experiments with commonly available profile data.

An interactive graphical user interface (GUI) software is available for download as part of the supplementary materials provided at http://pages.jh.edu/~cmeneve1/datasets.html.

Acknowledgements

REFERENCES

BAARS, W. J., SQUIRE, D. T., TALLURU, K. M., ABBASSI, M. R., HUTCHINS, N. & MARUSIC, I. 2016 Wall-drag measurements of smooth- and rough-wall turbulent boundary layers using a floating element. *Exp. Fluids* **57** (5), 90.

BRZEK, B., CAL, R. B., JOHANSSON, G. & CASTILLO, L. 2007 Inner and outer scalings in rough surface zero pressure gradient turbulent boundary layers. *Phys. Fluids* **19** (6), 065101.

CASTRO, I. P. 2007 Rough-wall boundary layers: mean flow universality. *J. Fluid Mech.* **585**, 469–485.

CHAUHAN, K. A., MONKEWITZ, P. A. & NAGIB, H. M. 2009 Criteria for assessing experiments in zero pressure gradient boundary layers. *Fluid Dyn. Res.* **41** (2), 021404.

CHENG, H. & CASTRO, I. P. 2002 Near wall flow over urban-like roughness. *Boundary-Layer Meteorol.* **104**, 229–259.

CHENG, H., HAYDEN, P., ROBINS, A. G. & CASTRO, I. P. 2007 Flow over cube arrays of different packing densities. *J. Wind Engng Ind. Aerodyn.* **95** (8), 715–740.

CLAUS, J., KROGSTAD, P. A. & CASTRO, I. P. 2012 Some measurements of surface drag in urban-type boundary layers at various wind angles. *Boundary-Layer Meteorol.* **145** (3), 407–422.

CLAUSER, F. H. 1954 Turbulent boundary layers in adverse pressure gradients. *J. Aero. Sci.* **21** (2), 91–108.

COLES, D. 1956 The law of the wake in the turbulent boundary layer. *J. Fluid Mech.* **1** (2), 191–226.

FERREIRA, M. A., RODRIGUEZ-LOPEZ, E. & GANAPATHISUBRAMANI, B. 2018 An alternative floating element design for skin-friction measurement of turbulent wall flows. *Exp. Fluids* **59** (10), 155.

FUKAGATA, K., IWAMOTO, K. & KASAGI, N. 2002 Contribution of Reynolds stress distribution to the skin friction in wall-bounded flows. *Phys. Fluids* **14** (11), L73–L76.

HARITONIDIS, J. H. 1989 The measurement of wall shear stress. In *Advances in Fluid Mechanics Measurements*, pp. 229–261. Springer.

JACKSON, P. S. 1981 On the displacement height in the logarithmic velocity profile. *J. Fluid Mech.* **111**, 15–25.

KEIRSBULCK, L., LABRAGA, L., MAZOUZ, A. & TOURNIER, C. 2002 Surface roughness effects on turbulent boundary layer structures. *J. Fluids Engng* **124**, 127–135.

KLEWICKI, J. C., SARIC, W. S., MARUSIC, I. & EATON, J. K. 2007 Wall-bounded flows. In *Springer Handbook of Experimental Fluid Mechanics*, pp. 871–907. Springer.

KROGSTAD, P. A. & EFROS, V. 2010 Rough wall skin friction measurements using a high resolution surface balance. *Intl J. Heat Fluid Flow* **31** (3), 429–433.

LI, J. D., HENBEST, S. M. & PERRY, A. E. 1986 The difficulties in the measurements of Reynolds stresses in smooth- and in rough-wall turbulent boundary layers. In *9th Australasian Fluid Mechanics Conference, Auckland, New Zealand*, pp. 456–459.

MEHDI, F., JOHANSSON, T. G., WHITE, C. M. & NAUGHTON, J. W. 2014 On determining wall shear stress in spatially developing two-dimensional wall-bounded flows. *Exp. Fluids* **55** (1), 1656.

MEHDI, F. & WHITE, C. M. 2011 Integral form of the skin friction coefficient suitable for experimental data. *Exp. Fluids* **50** (1), 43–51.

MORRILL-WINTER, C., KLEWICKI, J., BAIDYA, R. & MARUSIC, I. 2015 Temporally optimized spanwise vorticity sensor measurements in turbulent boundary layers. *Exp. Fluids* **56** (12), 216.

MORRILL-WINTER, C., SQUIRE, D. T., KLEWICKI, J. C., HUTCHINS, N., SCHULTZ, M. P. & MARUSIC, I. 2017 Reynolds number and roughness effects on turbulent stresses in sandpaper roughness boundary layers. *Phys. Rev. Fluids* **2**, 054608.

NAKAGAWA, S. & HANRATTY, T. J. 2001 Particle image velocimetry measurements of flow over a wavy wall. *Phys. Fluids* **13** (11), 3504–3507.

PERRY, A. E. & JOUBERT, P. N. 1963 Rough-wall boundary layers in adverse pressure gradients. *J. Fluid Mech.* **17** (2), 193–211.

PERRY, A. E. & LI, J. D. 1990 Experimental support for the attached-eddy hypothesis in zero-pressure-gradient turbulent boundary layers. *J. Fluid Mech.* **218**, 405–438.

PLACIDI, M. & GANAPATHISUBRAMANI, B. 2015 Effects of frontal and plan solidities on aerodynamic parameters and the roughness sublayer in turbulent boundary layers. *J. Fluid Mech.* **782**, 541–566.

PLACIDI, M. & GANAPATHISUBRAMANI, B. 2018 Turbulent flow over large roughness elements: effect of frontal and plan solidity on turbulence statistics and structure. *Boundary-Layer Meteorol.* **167** (1), 99–121.

PLACIDI, M. & GANAPATHISUBRAMANI, B. 2019 Velocity statistics for rough-wall turbulent boundary layer flow over lego roughness elements in different layouts. University of Southampton. doi:10.5258/SOTON/D0829.

RAUPACH, M. R., ANTONIA, R. A. & RAJAGOPALAN, S. 1991 Rough-wall turbulent boundary layers. *Appl. Mech. Rev.* **44**, 1–25.

REYNOLDS, R. T. & CASTRO, I. P. 2008 Measurements in an urban-type boundary layer. *Exp. Fluids* **45**, 141–156.

ROTTA, J. C. 1962 Turbulent boundary layers in incompressible flow. *Prog. Aerosp. Sci.* **2** (1), 1–95.

SCHLICHTING, H. 1979 *Boundary Layer Theory*, 7th edn. McGraw-Hill.

SCHULTZ, M. P. & FLACK, K. A. 2007 The rough-wall turbulent boundary layer from the hydraulically smooth to the fully rough regime. *J. Fluid Mech.* **580**, 381–405.

SILLERO, J. A., JIMÉNEZ, J. & MOSER, R. D. 2013 One-point statistics for turbulent wall-bounded flows at Reynolds numbers up to $\delta^{+} \approx 2000$. *Phys. Fluids* **25**, 105102.

SQUIRE, D. T., MORRILL-WINTER, C., HUTCHINS, N., SCHULTZ, M. P., KLEWICKI, J. C. & MARUSIC, I. 2016 Comparison of turbulent boundary layers over smooth and rough surfaces up to high Reynolds numbers. *J. Fluid Mech.* **795**, 210–240.

VOLINO, R. J. & SCHULTZ, M. P. 2018 Determination of wall shear stress from mean velocity and Reynolds shear stress profiles. *Phys. Rev. Fluids* **3**, 034606.

WALKER, J. M. 2014 The application of wall similarity techniques to determine wall shear velocity in smooth and rough wall turbulent boundary layers. *J. Fluids Engng* **136** (5), 051204.

WEI, T., SCHMIDT, R. & MCMURTRY, P. 2005 Comment on the Clauser chart method for determining the friction velocity. *Exp. Fluids* **38** (5), 695–699.

WINTER, K. G. 1979 An outline of the techniques available for the measurement of skin friction in turbulent boundary layers. *Prog. Aerosp. Sci.* **18**, 1–57.

WU, Y. & CHRISTENSEN, K. T. 2007 Outer-layer similarity in the presence of a practical rough-wall topography. *Phys. Fluids* **19** (8), 085108.